Multiscale experimental investigation of crystal plasticity and grain boundary sliding in synthetic halite using digital image correlation

Mathieu Bourcier, Michel Bornert, Alexandre Dimanov, Eva Héripré, Jean Raphanel

JOURNAL OF GEOPHYSICAL RESEARCH: SOLID EARTH, VOL. 118, 511–526, doi:10.1002/jgrb.50065, 2013

Multiscale experimental investigation of crystal plasticity and grain boundary sliding in synthetic halite using digital image correlation

M. Bourcier,[1] M. Bornert,[2] A. Dimanov,[1] E. Héripré,[1] and J. L. Raphanel[1]

Received 20 September 2012; revised 14 December 2012; accepted 19 December 2012; published 19 February 2013.

[1] There is a renewed interest in the study of the rheology of halite since salt cavities are considered for waste repositories or energy storage. This research benefits from the development of observation techniques at the microscale, which allow precise characterizations of microstructures, deformation mechanisms, and strain fields. These techniques are applied to uniaxial compression tests on synthetic halite done with a classical press and with a specific rig implemented in a scanning electron microscope. Digital images of the surface of the sample have been recorded at several loading stages. Surface markers allow the measurement of displacements by means of digital image correlation techniques. Global and local strain fields may then be computed using ad hoc data processing. Analysis of these results provides a measure of strain heterogeneity at various scales, an estimate of the size of the representative volume element, and most importantly an identification of the deformation mechanisms, namely crystal slip plasticity and grain boundary sliding, which are shown to be in a complex local interaction. Indeed, the applied macroscopic loading gives rise locally to complex stress states owing to relative crystallographic orientations, density and orientation of interfaces, and local deformation history. We have quantitatively estimated the relative importance of crystal slip plasticity and grain boundary sliding for different microstructures and evidenced their dependence on grain size. The two mechanisms of deformation and their link to the microstructure should thus be considered when modeling polycrystalline viscoplasticity.

Citation: Bourcier, M., M. Bornert, A. Dimanov, E. Héripré, and J. L. Raphanel (2013), Multiscale experimental investigation of crystal plasticity and grain boundary sliding in synthetic halite using digital image correlation, *J. Geophys. Res. Solid Earth*, *118*, 511–526, doi:10.1002/jgrb.50065.

1. Introduction

[2] The mechanical properties of halite have been extensively studied over several decades, because halite is a rock forming mineral with geotechnical and industrial applications. Geological storage of liquid and gaseous hydrocarbons in deep caverns is a worldwide current situation [*Carter and Hansen*, 1983; *Bérest et al*., 2005], and the potential for geological storage of nuclear wastes in deep salt mines is strongly envisaged by some countries, for instance Germany or the United States. These studies, mostly based on macroscopic mechanical testing, aim at the characterization of the macroscopic behavior of halite and the derivation of phenomenological constitutive relations (see for instance, *Senseny et al*. [1992]; *Langer* [1984]).

[3] More recently, in the frame of the compressed air energy storage projects [*Crotogino et al*., 2001], salt caverns have been considered for the storage of "green energy" in the form of compressed air. The specifics of these new projects, namely low overall stress levels, cyclic loading with short characteristic times, temperature and humidity fluctuations, have pointed out the limits of a purely phenomenological approach, and motivated micromechanical investigations for which the experimental identification of the physical mechanisms associated with the deformation of the material is the foundation of the modeling effort.

[4] Despite the fact that recent investigations of natural rock salts [*Schléder et al*., 2007; *Desbois et al*., 2010] provide significant insights on the active deformation mechanisms in natural conditions, the natural material is however not well suited for our experiments, which require small samples, a good reproducibility, controlled composition, and microstructure, i.e., grain size distribution, porosity, water content. Consequently, in our study, as in many other laboratory investigations, synthesized halite has been used. This may be done at a relatively low cost, starting with pure

[1]Laboratoire de Mécanique des Solides, CNRS UMR 7649, École Polytechnique, 91128, Palaiseau Cedex, France.
[2]Laboratoire Navier, Université Paris-Est, CNRS UMR 8205, École des Ponts ParisTech, 77455, Marne la Vallée Cedex 2, France.

Corresponding author: J. L. Raphanel, Laboratoire de Mécanique des Solides, CNRS UMR 7649, École Polytechnique, 91128 Palaiseau Cedex, France. (raphanel@lms.polytechnique.fr)

2169-9313/13/10.1002/jgrb.50065

NaCl powder and using thermomechanical treatments tuned to provide the desired final microstructure.

[5] Unlike most rock forming minerals, halite has a viscoplastic behavior with measurable characteristic strain rates at fairly low deviatoric stresses even at room temperature. It is therefore a very convenient mineral and rock analogue for the experimental investigation of single crystal and polycrystal rheology. Moreover, being a very soluble mineral, in addition to the classical crystal plasticity (intracrystalline slip and/or dislocation creep), it allows to investigate solution-precipitation mediated creep [*de Meer et al*., 2002; *Skvortsova*, 2003], which is a very active mechanism in natural environments, in the presence of fluids and at low temperatures and stresses, like in diagenetic settings.

[6] For these reasons, halite has also been a material of choice over several decades for the purpose of academic investigations. For example, experimentally deformed halite has been used to test analytical scale transition models, designed to predict the effective overall polycrystalline behavior from the single crystal's plastic deformation mechanisms, taking into account texture evolutions and dynamic recrystallization [*Wenk et al*., 1989; *Lebensohn et al*., 2003; *Liu et al*., 2005; *Wenk et al*., 2009]. The understanding of pressure-solution creep in itself, and its contribution to the whole rheology as a possible accommodation mechanism, has been greatly improved thanks to experimental studies of halite compaction, creep and recrystallization [*Urai et al*., 1986, 1987; *Peach and Spiers*, 1996; *Hickman and Evans*, 1995; *Spiers and Schutjens*, 1999; *Martin et al*., 1996; *Ter Heege et al*., 2005; *Schenk et al*., 2006; *Watanabe*, 2010].

[7] Synthetic halite can similarly be considered in the present study as an analogue material for the general investigation of the viscoplastic behavior of polycrystals exhibiting several concurrent or competing deformation mechanisms. We more specifically focus the investigation on the dependence of the relative activation of these mechanisms with microstructure and especially grain size. To do so, we apply innovative micromechanical experimental investigations to identify the different micromechanisms activated during plastic deformation under uniaxial conditions and to understand their interactions. Conventional uniaxial compression tests, combined with optical observation, as well as tests with a specific loading device fitted inside a scanning electron microscope (SEM) have been run. This combination of techniques allows direct surface observation over a wide range of scales, going from the single crystal (or grain) to the multicrystal (or aggregate with a few dozens of grains) and the polycrystal (hundreds or thousands of grains). In all experiments, optical or electron digital images have been recorded at several consecutive loading stages and compared by digital image correlation (DIC) to compute the full heterogeneous strain fields at these different scales of observation. This procedure provides a direct qualitative visualization of the active micromechanisms, but also, thanks to a specific postprocessing procedure, a quantification of their respective contributions to the overall strain.

[8] Elaboration routes to synthetize halite with various controlled microstructures are presented in the next section. Micromechanical experimental methods are then described in section 3, with a special emphasis on the definition and computation of strains at various scales. Section 4 is devoted to a systematic but mostly qualitative comparison of the deformation modes of three halite samples with different microstructures, observed at various scales. The discussion in section 5 will lead to the proposition and the first application of a new procedure to quantitatively compare the relative contributions of crystal slip plasticity (CSP) and grain boundary sliding (GBS) to the overall deformation.

2. Sample Preparation

[9] To obtain a controlled composition and microstructure, we use as raw material a commercial NaCl powder of laboratory purity (Normapur reagent grade 99.9% pure, Prolabo). The variability of the synthetic samples will thus be very low compared to natural samples, which is particularly important when testing small samples. The grain size and grain size distribution are the microstructural parameters that we wish to control through the thermomechanical processes of elaboration because they have been shown to be very important in determining the dominant deformation mechanisms and the heterogeneity of the strain fields [*Dimanov et al*., 2003]. We have therefore chosen to prepare three kinds of materials, characterized by large grains, fine grains, and a bimodal distribution of large and small grains.

[10] Samples are obtained by pressing the sodium chloride powder for 48 h under an axial load of 100 MPa in a steel cylinder mounted on a hydromechanical press (MTS system). The compacted material is then hot-pressed for one week at 150°C at same axial load. The whole piston-cylinder device is externally heated in an oven adapted to the press. The typical core-sample dimensions after hot-pressing are about 11 cm in height and 8 cm in diameter. This material (that will be further referred to as "hot-pressed") has good cohesion and low porosity (estimated between 1 to 3% in volume, by Archimedes weighing in petrol). However, the grain size distribution is widespread and ranges from 80 to 400 μm (Figure 1a).

[11] Some core-samples are subsequently annealed at atmospheric pressure, for 48 h in an oven at 750°C, which results in larger average grain sizes, ranging from 250 to 500 μm (Figure 1b) and a narrow grain size distribution. The annealed material will be called "coarse-grained" in the following. Its grains have polygonal shapes, mostly equiaxed, with rather straight grain boundaries. Their porosity is less than 3% in volume.

[12] A third microstructure is obtained by adding an initial stage of crushing and ball milling the NaCl powder, then performing an extended cold-pressing phase for one week, followed by hot-pressing but no annealing as for the first microstructure. To limit crystal growth during hot-pressing, 3% volume copper particles with a diameter of about 10 μm have been mixed with the initial NaCl powder [*Dresen and Evans*, 2009]. These samples have grain sizes between 30 and 80 μm and will be called "fine-grained" (Figure 1c). Their porosity is about 1% in volume.

[13] The water content has not been systematically measured. However, we may assume that the hot-pressing procedure eliminates most of the water that may have been adsorbed by the initial powder. All the macroscopic mechanical tests are realized in similar conditions of ambient humidity, and the microscopic tests are performed in a SEM under high vacuum.

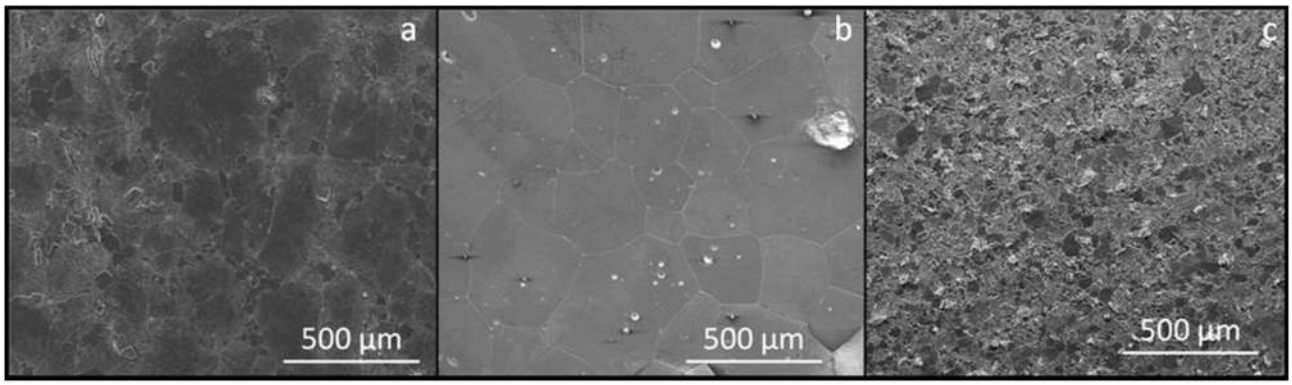

Figure 1. Different microstructures: (a) hot pressed, (b) coarse-grained, (c) fine-grained.

[14] Results of standard macroscopic tests, triaxial creep, and uniaxial compression, on our synthetized materials confirm that their global mechanical properties fall in line with those of common natural halites [*Franssen*, 1994].

3. Methods

3.1. Macroscopic Tests

[15] The uniaxial compression loading is applied by an electromechanical press, with 100 kN capacity. The cylindrical samples (23.55 mm in height and 22.9 mm in diameter) are directly cored from the hot-pressed material. To minimize frictional effects, we have placed Teflon layers between the sample's ends and the steel platens. Two diametrically opposed flat surfaces are machined on the cylindrical sample parallel to its axis, with a width of 15 mm. These surfaces are polished and spray painted with black matte paint for the purpose of optical DIC. An optical system based on a 16 Mpixel camera with a pixel width of 7.4 µm and with an optical magnification close to unity records images of the whole observation surface. Details of the optical setup can be found in *Yang et al.* [2010, 2012]. The sample is loaded at a constant displacement rate of 1 $\mu m \cdot s^{-1}$, corresponding to a strain rate of about $4.10^{-5}\ s^{-1}$. Digital images are recorded every second.

3.2. In Situ Scanning Electron Microscope Tests

[16] The micromechanical (or "microscopic") uniaxial loading tests are performed inside the chamber of a Field Emission Gun SEM (FEI Quanta 600). The SEM is equipped with a miniaturized deformation stage developed in the laboratory, which operates at chosen constant displacement rates. In our case, the samples, about 12 mm in length and with a $6 \times 6\ mm^2$ cross-section, are loaded in compression at $1\ \mu m \cdot s^{-1}$, corresponding to a strain rate of about $8.10^{-5} s^{-1}$. The sample's surfaces are metallized with a thin gold film to avoid surface charging during secondary electron imaging in high vacuum mode. High definition pictures (4096×3775 pixels) with a sufficiently low noise level are recorded with a dwell time of about 20 µs, leading to a total recording time of about 350 s per image, during which the loading is stopped.

3.3. Digital Image Correlation

[17] Digital image correlation is an experimental method based on the comparative processing of digital images, which are the successive representations of the states of evolution of a given experimental process. It aims at extracting quantitative information about this evolution on the basis of the changes detected from one image to another. In a general sense, DIC may be applied to any kind of imaging technology. It has originally been developed for macroscopic optical observations [*Sutton et al.*, 1983] and a large number of applications can be found in literature in this context. Extensions to other two-dimensional (2D) imaging techniques, including optical microscopy, scanning electron microscopy and atomic force microscopy, as well as to three-dimensional imaging techniques such as X-rays computed tomography and microtomography, have been proposed during recent years [*Sutton et al.*, 2009; *Bornert et al.*, 2011]. The combination of DIC with optical microscopy (OM) or SEM turns out to be a particularly efficient tool for the micromechanical investigation of the mechanical behavior of a wide range of man-made or natural materials. Strain fields can be measured at the scale of their heterogeneous microstructure, to not only identify local deformation and damage mechanisms acting at microscale, but also quantify their interactions over large domains representative of their heterogeneity. Recent applications address the behavior of ductile metals [*Doumalin and Bornert*, 2000; *Doumalin et al.*, 2003; *Tatschl and Kolednik*, 2003; *Héripré et al.*, 2007; *Gérard et al.*, 2009] as well as of geomaterials, like argillaceous rocks [*Bornert et al.*, 2010; *Hedan et al.*, 2012] or brittle carbonates [*Dautriat et al.*, 2011].

[18] In the present case, both OM and SEM are used to investigate the multiscale nature of the local strain in halite, over an unprecedented wide range of scales. Indeed optical observations allow capturing the heterogeneity of the strain field on the above described macroscopic samples at scales ranging from the centimetric sample's size down to about 100 µm, while the complementary SEM investigations on the parallelepipedic samples cover scales ranging from a few millimeters to a few micrometers. The digital image processing is carried out with the in-house software CMV developed in LMS and Navier laboratories, which has demonstrated its versatility for a wide range of applications.

[19] The DIC technique aims at measuring a displacement field by the comparison of a reference image of the undeformed sample with images recorded after each deformation increment. The principle of the method [*Sutton et al.*, 2009; *Bornert et al.*, 2011] is to locate in the "deformed" images the "correlation windows" representing local areas of the sample (a few pixels in width), initially defined in the "reference"

image, with the assumption that the gray levels distribution in these windows is preserved during the transformation associated with the deformation. This procedure is automated and based on the optimization of a correlation criterion, which measures the similarity of the correlation windows in the two images, with respect to the parameters characterizing the transformation. Once this operation is performed for a large number of correlation windows regularly distributed over a region of interest (ROI), the obtained discrete displacement field permits the computation of a strain field by means of appropriate differentiation procedures. In the present case, the principles described by *Allais et al*. [1994] are used to compute the in-plane components of the deformation gradient **F** relative to various gage lengths, from which various strain components can be derived, as described more precisely in section 3.5.

3.4. Surface Markers

[20] The application of DIC principles requires the existence of a sufficiently pronounced local contrast in the images at the scale of the correlation windows. Therefore, correlation windows cannot be smaller than a typical size of the marker, which creates the local contrast [*Bornert et al*., 2009]. On the other hand, this typical size needs to be sufficiently large to be resolved by the imaging technique. The polished surfaces of our synthetic halite samples do not present enough natural contrast to allow fine-scale image correlation. In such a case, one resorts to the deposition of appropriate surface markers and several techniques are available according to the sample size and the scale of interest.

[21] For the macroscopic tests performed under optical observation, one classically sprays matte black paint droplets (< 100 μm) [*Dautriat et al*., 2011] on the sample's surface (Figure 2a). For the microscopic tests performed in the SEM, aimed at the observation of local mechanisms of plasticity active at scales smaller than grain size, the size of the markers has to be significantly smaller than the size of the grains. In our case, marker sizes in the 1 to 10 μm range are expected. For metals, a standard fine-marking technique is based on electron beam microlithography, which uses a lithographic technique to print a periodic grid on the surface of the sample [*Allais et al*., 1994; *Héripré et al*., 2007].

[22] For the material under consideration, a new method has been developed to mark the surface at the micrometer scale, which turns out to be more efficient than lithography. We start by depositing a very thin gold film (thickness of about 30 nm) using a standard evaporator for surface metallization. Then, the metallized samples are annealed at 450°C under atmospheric pressure for 24 h. During annealing, the thin gold film experiences dewetting and micron-sized gold droplets progressively form at the surface of the sample (Figure 2b). The microstructures do not evolve, because the temperature is not high enough to allow significant grain growth. This marking procedure has several advantages, the first being its relative simplicity. In addition, it leaves the sample surface unaltered and provides homogeneously distributed and extremely fine-scaled markers with a typical size of the droplets of 1 μm, sufficiently small to investigate strain fields at micrometric gage lengths yet still larger than the pixel size of SEM images at the considered magnifications and image definitions. Another property of this marking is the random nature of the spatial distribution of the markers and its higher density of gray level contrast, compared to a microgrid. This can facilitate the application of digital image correlation procedures and improve their accuracy.

3.5. Strain Computation

[23] This section is devoted to the definition of the strain measurement used to characterize the deformation of halite at various scales and to the description of the practical implementation of these concepts in the DIC software CMV. More details can be found in *Allais et al*. [1994]. One starts with a quick recall of the standard Lagrangian approach of continuum mechanics [*Malvern*, 1969; *Salençon*, 2001] according to which the mechanical transformation of a body is characterized by a bijective mapping Φ which relates the position $\mathbf{X}$ of some material particle in a reference or initial configuration to its position $\mathbf{x}$ in the current or deformed one

$$\mathbf{x} = \Phi(\mathbf{X}) \tag{1}$$

so that the displacement between current and reference positions is

$$\mathbf{u}(\mathbf{X}) = \mathbf{x} - \mathbf{X} = \Phi(\mathbf{X}) - \mathbf{X}. \tag{2}$$

[24] The deformation gradient $\mathbf{F}$ is the second-order tensor given by

$$\mathbf{F} = \frac{\partial \mathbf{x}}{\partial \mathbf{X}}, \tag{3}$$

which may also be written as

$$\mathbf{F} = \frac{\partial \Phi}{\partial \mathbf{X}} \quad \text{or} \quad \mathbf{F} = \frac{\partial \mathbf{u}}{\partial \mathbf{X}} + \mathbf{1}, \tag{4}$$

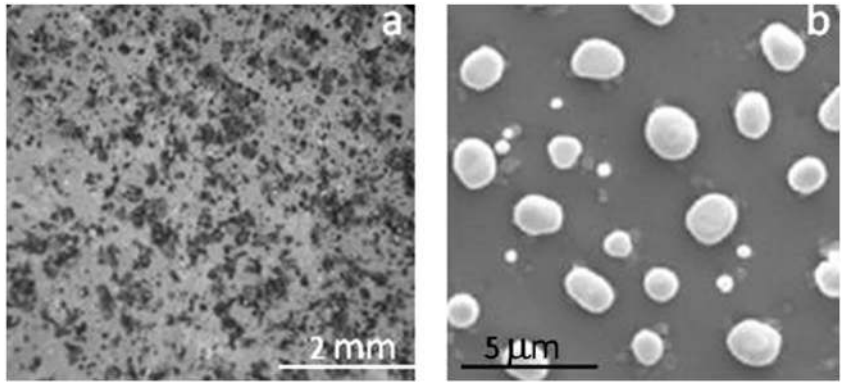

Figure 2. Two types of markers: (a) spray painting (optical image) and (b) microdroplets of gold (SEM micrograph).

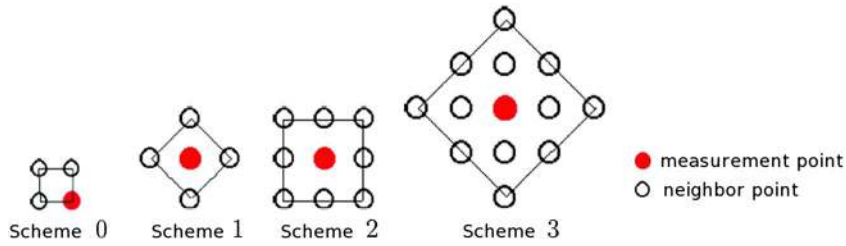

Figure 3. Different integration schemes for local strain computation. Scheme 0 will yield very local deformation, but with large uncertainty. Scheme 3 deformation will be less local but more accurate.

where 1 stands for the second-order identity tensor. It describes the transport in the neighborhood of $\mathbf{X}$ of any infinitesimal material vector $\mathbf{dX}$ according to

$$\mathbf{dx} = \mathbf{F}(\mathbf{X})\cdot\mathbf{dX}. \tag{5}$$

[25] A standard appropriate measure of strain, providing the variations of lengths and angles, is the Green-Lagrange strain tensor $\mathbf{E}$ defined by

$$\mathbf{E}(\mathbf{X}) = \frac{1}{2}\left(\mathbf{F}^T\cdot\mathbf{F} - \mathbf{1}\right), \tag{6}$$

where superscript "T" denotes the transpose of a tensor. When the strains and rigid body rotations remain small, typically a few percents and a few degrees respectively, a linearized expression of $\mathbf{E}$ may be preferred, which is the usual "small strain tensor"

$$\boldsymbol{\varepsilon} = \frac{1}{2}\left(\mathbf{F}^T + \mathbf{F}\right) - \mathbf{1} = \frac{1}{2}\left(\left(\frac{\partial \mathbf{u}}{\partial \mathbf{X}}\right)^T + \frac{\partial \mathbf{u}}{\partial \mathbf{X}}\right). \tag{7}$$

[26] We thus see that these standard definitions of strain strongly depend on the calculation of the gradient (3). In practice, its evaluation has to overcome two difficulties. The first more practical one is related to the fact that the displacement field $\mathbf{u}$ is measured on a discrete set of points so that its derivative cannot be known exactly and has to be estimated by some finite difference. In addition, and more fundamentally, it is noted that the derivative (3) is not well defined as a consequence of the multiscale nature of the transformation, which induces very strong fluctuations of $\mathbf{F}(\mathbf{X})$ with $\mathbf{X}$ and a dependence of $\mathbf{F}(\mathbf{X})$ with the scale of the infinitesimal material vector $\mathbf{dX}$ used in relation (5). This point will be illustrated further by our experimental results in section 4.

[27] To circumvent these difficulties, it is proposed to replace the theoretical derivative (3) by a finite difference with respect to some specified gage length ΔL. For a one-dimensional function f, one may then define its derivative relative to this gage length as

$$\left(\frac{df}{dX}\right)_{\Delta L}(X) = \frac{f(X + \Delta L/2) - f(X - \Delta L/2)}{\Delta L}. \tag{8}$$

[28] This quantity can be computed from discrete experimental measurements of f as long as these measurements are performed on a regularly spaced set of points with a ΔL spacing. Such a definition of the "ΔL -derivative" of f coincides clearly with the spatial average over the domain $D(X) = [X + \Delta L/2, X + \Delta L/2]$ of the classical gradient

$$\left(\frac{df}{dX}\right)_{\Delta L}(X) = \frac{f(X + \Delta L/2) - f(X - \Delta L/2)}{\Delta L} = \frac{1}{\Delta L}\int_{X-\Delta L/2}^{X+\Delta L/2}\frac{df}{dX}(v)dv = <\frac{df}{dX}>_{D(X)}, \tag{9}$$

which can unambiguously be defined and computed.

[29] This "weak" unidimensional definition of derivation can readily be extended to the tensor quantities needed for the characterization of surface strains and deduced from the in-plane components of the displacement field. The local deformation gradient at point $\mathbf{X}$ with respect to some surface S is defined as the average of the infinitesimal gradient over the surface S centered on point $\mathbf{X}$, and can be transformed into a contour integral by application of Green's theorem

$$\mathbf{F}^S(\mathbf{X}) = <\mathbf{F}>_{S(\mathbf{X})} = \frac{1}{|S(\mathbf{X})|}\int_{\partial S(\mathbf{X})}\Phi(\mathbf{v})\otimes\mathbf{n}(\mathbf{v})dl_{\mathbf{v}}, \tag{10}$$

where $|S|$ is the measure of the domain S, ∂S its closed contour, and $\mathbf{n}(\mathbf{v})$ the outward normal to the contour $\partial S(\mathbf{X})$.

[30] In practice, the contour $\partial S(\mathbf{X})$ is chosen as a polygonal path whose vertices coincide with measurement points in the vicinity of the position $\mathbf{X}$ where the gradient is evaluated and the transformation $\Phi(\mathbf{v})$ is linearly interpolated between two neighboring positions. Various contours are defined in CMV on a regularly spaced grid of displacement measurement points, as illustrated in Figure 3. The corresponding local strain gage length (referred to as ΔL in the following) is for convenience defined as the length of the sides of the obtained squares (e.g., $\Delta L = 1$ grid step for scheme 0 and $\Delta L = 2\sqrt{2}$ grid steps for scheme 3). These assumptions allow replacing the integral (10) by the following discrete sums [*Allais et al.*, 1994] for each in-plane component of the deformation gradient $\mathbf{F}^S$, relative to the (x,y) directions, which coincide with the axes of the reference image:

$$\begin{aligned} F^S_{xx} &= <F_{xx}>_S = \frac{1}{2|S|}\sum_{n=1}^{N} x_n(Y_{n+1} - Y_{n-1}) \\ F^S_{xy} &= <F_{xy}>_S = \frac{1}{2|S|}\sum_{n=1}^{N} x_n(X_{n+1} - X_{n-1}) \\ F^S_{yx} &= <F_{yx}>_S = \frac{1}{2|S|}\sum_{n=1}^{N} y_n(Y_{n+1} - Y_{n-1}) \\ F^S_{yy} &= <F_{yy}>_S = \frac{1}{2|S|}\sum_{n=1}^{N} y_n(X_{n+1} - X_{n-1}) \end{aligned}, \tag{11}$$

where (x_n,y_n) are the coordinates of the n^{th} contour point in the deformed configuration, measured by DIC, and (X_n,Y_n)

the coordinates of the n^{th} point in the initial configuration, chosen in the reference image (note that in these relations, for convenience, the $(N+1)^{th}$ point coincides with the first one, and the 0^{th} point with the last one).

[31] The Green-Lagrange strain tensor $\mathbf{E}^S(\mathbf{X})$ relative to local surface S is deduced from $\mathbf{F}^S$ by relation (6) in which $\mathbf{F}$ is substituted by $\mathbf{F}^S$. Note however that none of the components of $\mathbf{E}^S(\mathbf{X})$ can be evaluated exactly if the only known components of $\mathbf{F}^S$ are its in-plane components. One may however compute the in-plane components of the small strain tensor (and these components only) according to

$$\begin{aligned} \varepsilon^S_{xx} &= F^S_{xx} - 1, \\ 2\varepsilon^S_{xy} &= F^S_{xy} + F^S_{yx}, \\ \varepsilon^S_{yy} &= F^S_{yy} - 1. \end{aligned} \tag{12}$$

[32] Whenever needed, additional hypotheses have to be made to estimate the three missing components of this tensor. A convenient assumption is that the normal axis to the observation plane is a principal axis of the deformation and that there is no out of plane rotation, so that $\varepsilon_{zx} = \varepsilon_{zy} = 0$. An additional assumption is still needed to evaluate ε_{zz}. Three main choices are open: plane strain, $\varepsilon_{zz} = 0$, isochoric strain $\varepsilon_{zz} = -(\varepsilon_{xx} + \varepsilon_{yy})$, or uniaxial local strain (extension or contraction) $\varepsilon_{zz} = \varepsilon_2$ with $(\varepsilon_1, \varepsilon_2)$ the two in-plane principal strains, such that $|\varepsilon_2| \leq |\varepsilon_1|$. Knowing all six components of the small strain tensor, it may then be convenient to represent the deviatoric strain by a scalar such as the equivalent von Mises strain

$$\varepsilon_{\text{eq}} = \sqrt{\frac{2}{3}(\boldsymbol{\varepsilon}^{\mathbf{dev}} : \boldsymbol{\varepsilon}^{\mathbf{dev}})}, \tag{13}$$

where $\boldsymbol{\varepsilon}^{\mathbf{dev}}$ is the deviatoric part of $\boldsymbol{\varepsilon}$. Note that under the third assumption (uniaxial strain, adopted in the following), the von Mises strain coincides with

$$\varepsilon_{\text{eq}} = \frac{2}{3}|\varepsilon_1 - \varepsilon_2|, \tag{14}$$

which is also a measure of the deviatoric part of the in-plane strain tensor, independently of any assumption relative to the out-of-plane components of the gradient.

[33] These definitions of local deformation gradients and strain tensors can straightforwardly be extended to the definition of the corresponding quantities relative to any surface S. In particular, when S is extended to the whole ROI and ∂S discretized over the measurement points surrounding it, one gets the average deformation gradient and strain over this area. This is the way the strains are computed in section 4 to obtain the overall stress-strain curves. In addition, if the surface S is sufficiently large to encompass a whole representative volume element (RVE) but still small with respect to macroscopic fluctuations of the strain field, one gets the macroscopic deformation gradients and strain tensors, as discussed in more detail in section 4.2. When S coincides with a grain, the average deformation gradient and strain components over this grain are obtained. This latter case will be further discussed in section 5.

3.6. Strain Computation Accuracy

[34] Let us finally briefly comment on the accuracy of the evaluations (11) of the components of $\mathbf{F}^S$. In these relations, the (X_n, Y_n) components are chosen and the only measured quantities are the (x_n, y_n) coordinates. If the latter are obtained by DIC with nonoverlapping correlation windows, the experimental errors on these components will be independent. The standard deviations of the errors on the components of $\mathbf{F}^S$ can then be easily derived from those on the components (x_n, y_n), following relations given by *Allais et al*. [1994]. Errors on DIC evaluations of displacements depend on many factors, which cannot be discussed in detail here. We refer to *Wang et al*. [2009], *Bornert et al*. [2009, 2010], *Yang et al*. [2010], and *Dautriat et al*. [2011] for various recent discussions on this question and procedures to quantitatively evaluate these errors on similar setups. However, under the assumption that the displacement field can be described with sufficient accuracy by an affine shape function at the scale of the correlation windows as done in the CMV software, the DIC error will decrease when increasing the correlation window size. This assumption is reasonable for sufficiently small windows. It is thus of interest to choose window sizes that coincide with the grid spacing, so that correlation windows do not overlap but cover the whole images to take into account the whole information they carry. This is the practical choice made to obtain most of the results presented hereafter. In some cases, correlation window sizes may be smaller than grid spacing, but still large enough to ensure a sufficient accuracy, that is to say enough local contrast. In any case, DIC errors tend to be sufficiently small (by more than an order of magnitude) when compared to the levels of local and global strains computed from our experiments. For instance, one records a DIC error of 0.1% at an equivalent strain of 3%. Things are different for brittle rocks, which break at strain levels notably below 10^{-3} and for which specific optimization routines are required to reduce experimental noise, as described, e.g., by *Dautriat et al*. [2011]. In the present case, strain levels reach several percents, so that DIC accuracy is not really an issue, except for specific questions that will be discussed in section 5. It should finally be noted that the gage length ΔL relative to local strain measurements and the size of the correlation window are two quantities that are chosen separately and which do coincide only when the derivation scheme 0 is selected (see Figure 3) and with juxtaposed correlation windows. Unless otherwise specified, scheme 2 has been used in the present study. The choices of gage lengths and correlation window sizes used for the analyses of the various tests commented in the following section are summarized in Table 1. The pitch is the number of pixels between two consecutive points, hence with scheme 2, the gage length is twice the pixel size times the pitch.

4. Results

4.1. Multiscale Structure of the Strain Fields Evidenced on Macroscopic Tests

[35] Macroscopic tests have been made on each of the different materials. Let us first focus on the results of a macroscopic test performed on a synthetic hot-pressed sample with a bimodal grain size distribution: large grains of about 400

Table 1. Main DIC and Strain Computation Parameters Used for Each Microstructure

Test	Microstructure	Scale	Grain Size (μm)	Pixel Size (μm)	Pitch (pixels)	Scheme	Gage Length (μm)
1	Hot-pressed	macro	30–80/250–500	7.4	15	2	222
2	Hot-pressed	macro	30–80/250–500	7.4	120	2	1776
3	Hot-pressed	meso/micro	30–80/250–500	0.1	15	2	3
4	Coarse grained	meso	250–500	0.4	10	2	8
5	Coarse grained	micro	250–500	0.02	40	2	1.6
6	Fine grained	macro	30–80	0.3	30	2	18
7	Fine grained	macro/meso	30–80	0.1	30	2	6

μm in diameter and small grains around 50 μm or smaller (Figure 1a). The global uniaxial stress-axial strain curve (Figure 4 [2]), obtained from the load cell and average gradient computations from DIC data, as explained at the end of section 3.5, is typical of an elastoplastic behavior with moderate strain hardening. A first analysis of the local response of the material, based on a rather fine gage length ($\Delta L \approx 220$ μm, see line 1 in Table 1), which is made possible by the high definition of the optical camera used to monitor the strain field on macroscopic tests and the fine spray painting, reveals a strongly heterogeneous strain distribution (Figure 4 [3]), with some highly strained areas next to almost undeformed ones. A finer observation shows in fact two scales of heterogeneity. A very small one, with a typical size close to one millimeter is related to the localization of the deformation into numerous micro-bands, oriented more or less at 45° with respect to the compression axis. Another much larger one is linked to the size of the sample and to the imperfections related to the actual boundary conditions of the uniaxial compression test. The latter heterogeneity is the only one that remains when the strain gage length is extended to a size exceeding the finer-scale heterogeneity. This is illustrated by strain maps obtained with $\Delta L \approx 1800$ μm (Figure 4 [4]), which show two less deformed areas near the interfaces between the sample and the pistons. These areas are affected by friction effects despite the use of Teflon sheets. Conversely, the central part of the sample deforms more. These features result in two conjugate macroscopic deformation bands spreading across the whole sample. It is noteworthy that the strain heterogeneity is much less pronounced at the macroscale than at the microscale as illustrated by the differences of their respective color maps. In addition, these patterns are present from the beginning of the test and evolve mainly proportionally with the overall strain. In some areas, the strain tends to increase faster, localizing the deformation, when one considers the microscale heterogeneity. A closer observation shows that these areas are the locus of microcracks almost parallel to the loading direction.

[36] This first example illustrates the existence of various possible scales of analysis of a mechanical test. The most macroscopic one addresses the strain heterogeneities induced by the geometry of the sample and the actual boundary conditions applied by the testing device. For a perfect uniaxial compression test on a homogeneous sample, this heterogeneity would not exist. In our case, because of unavoidable friction effects at the contacts between sample and platens, there is some heterogeneity, but its magnitude remains small. When the strain gage length is reduced to a size close to the grain size, a finer scale of heterogeneity is evidenced. It is induced by the heterogenous response of the material at a microscale where various deformation and/or damage mechanisms coexist, compete, or interact. Their average contribution determines the constitutive

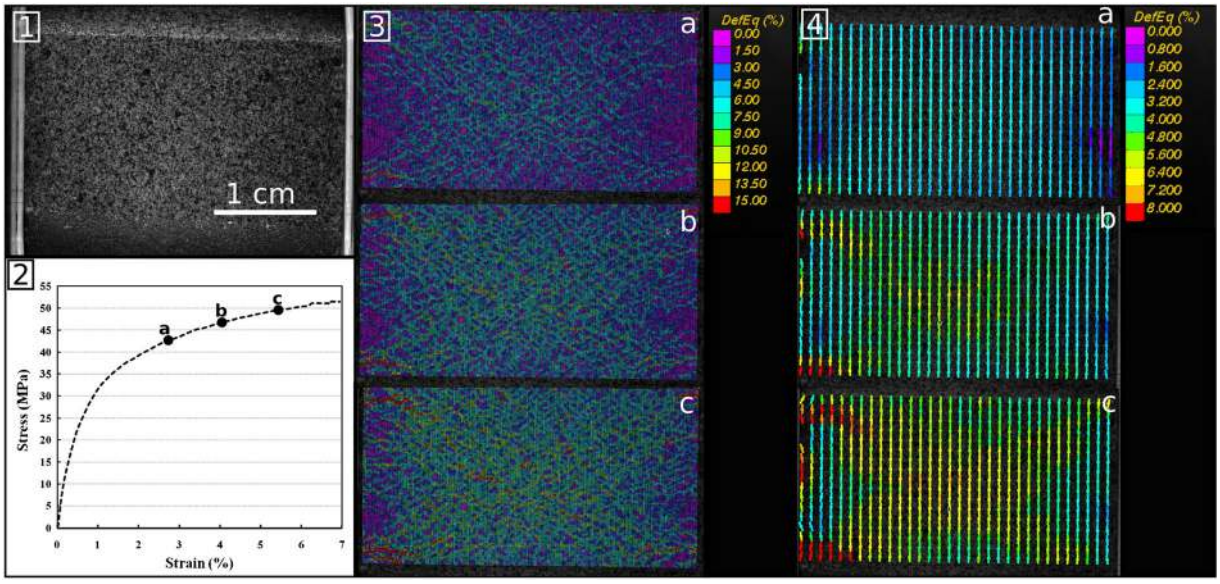

Figure 4. Optical 2D DIC results on a macroscopic sample of hot-pressed material. (1) Reference optical image with speckle painting. (2) Uniaxial stress / axial strain curve. Maps of equivalent strains relative to gage lengths (3)$\Delta L = 222$ μm and (4) $\Delta L = 1776$ μm, at the three stages of the test marked on (2).

behavior of the material. In the context of a micromechanical analysis of the latter, it is of highest interest to analyze this scale of heterogeneity of the local strain field, because it is the signature of the active physical mechanisms, their interactions, and their relative contributions to the overall deformation. For a correct evaluation of the latter, it is essential to extend the analysis over a domain sufficiently large to be representative of the statistics of these contributions, i.e., an RVE.

[37] In this context, the following analyses will be developed over three typical length scales: the so-called "macroscopic" analyses refer to situations where the ROI will be much larger than the RVE. If the strain gage length is sufficiently small with respect to the latter, the microscale heterogeneity will be emphasized, as in the example above with the smaller gage length; if not, only the macroscopic heterogeneity will be characterized. The "mesoscale" will refer to an investigation over an ROI with a size close to the one of the RVE and a gage length sufficiently small to reveal local strain fluctuations. Statistical analysis of these fluctuations will then be representative of the actual micromechanical behavior of the material. Finally, a "microscale" analysis will refer to a scale of investigation with a sufficiently high spatial resolution for a detailed investigation of a particular deformation mechanism, but spread over an area restricted to a few grains only and no longer representative of the material. At this scale, relative orientations (local texture) and grain morphology (size and shape) play crucial roles and are the sources of local strain heterogeneity. Local effects are linked to characteristic dimensions of the microstructure and are thus defined in a relative rather than an intrinsic way.

[38] The current state-of-the-art of imaging techniques does not allow covering all three scales within a single snapshot. However, the use of several image magnifications and, if necessary, several imaging techniques (OM and SEM in the present case) on the same material deformed at the same conditions allow such a multiscale investigation. This is what is proposed in the following on the three different microstructures: coarse-grained samples, fine-grained ones, and bimodal grain size distribution. In the following, the results are first commented from a qualitative point of view,

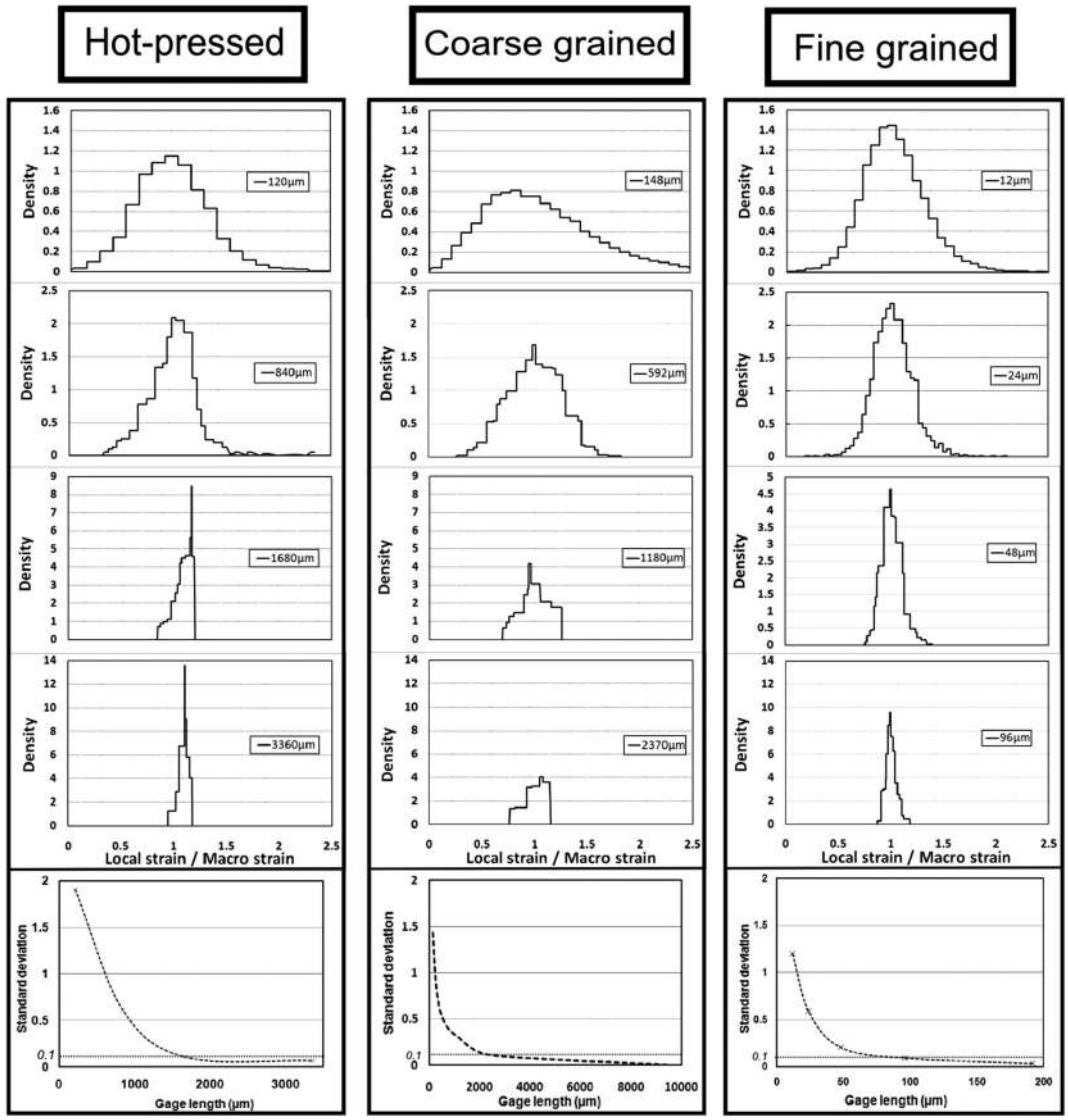

Figure 5. Strain distribution function for each material deduced from DIC measurements for various gage lengths ΔL and evolution of standard deviation with ΔL.

while a more quantitative investigation at mesoscale is outlined in section 5. It should be emphasized that the actual characteristic dimensions of these three scales of analysis depend on the microstructure under consideration. It is thus of high interest to quantify the size of an RVE, which is the purpose of the following section.

4.2. Quantification of Representative Volume Element Size From Strain Fields

[39] The representative volume element is a central concept for the micromechanical analysis of materials. There is an extensive literature addressing this question, and in particular the size of an RVE in relation to the characteristic

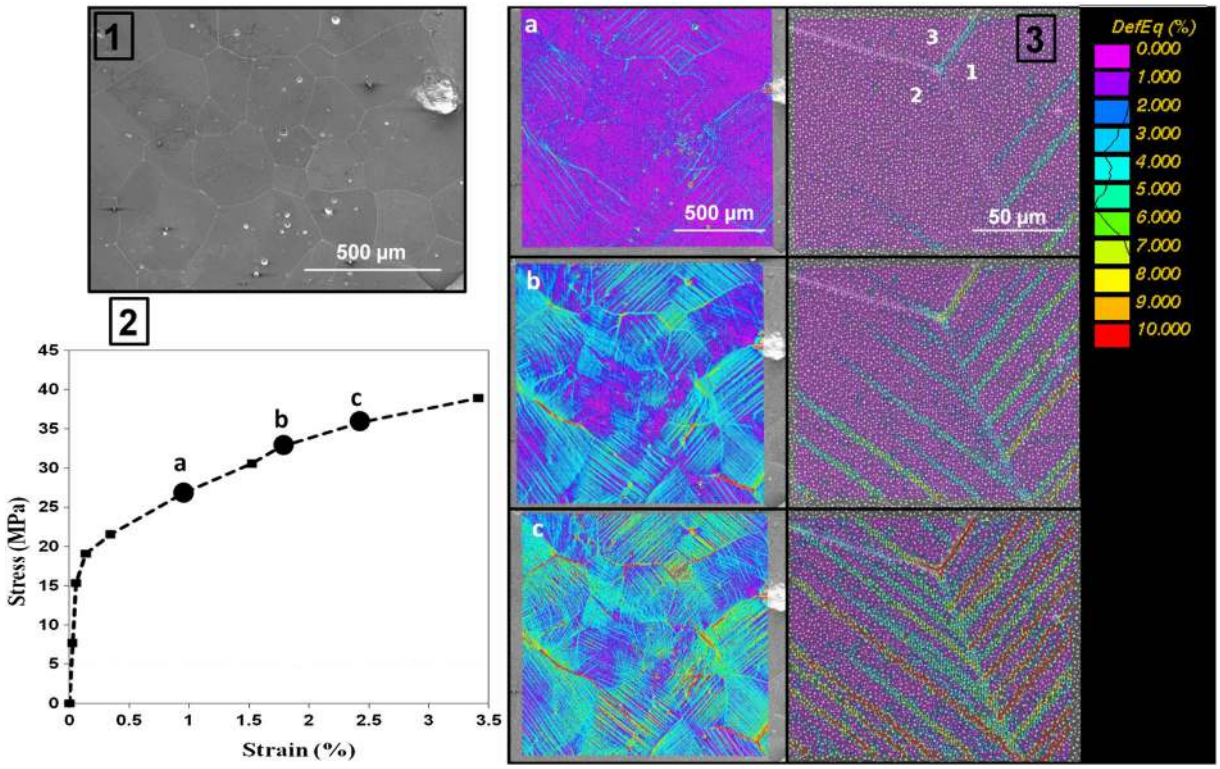

Figure 6. 2D DIC results from in situ SEM test on coarse-grained material. (1) Microstructure (SEM image). (2) Macroscopic stress/strain curve. (3) Equivalent strain maps at mesoscopic (left) and microscopic (right) scales. Intracrystalline slip bands develop inhomogeneously within individual grains, and grain boundary sliding is often observed.

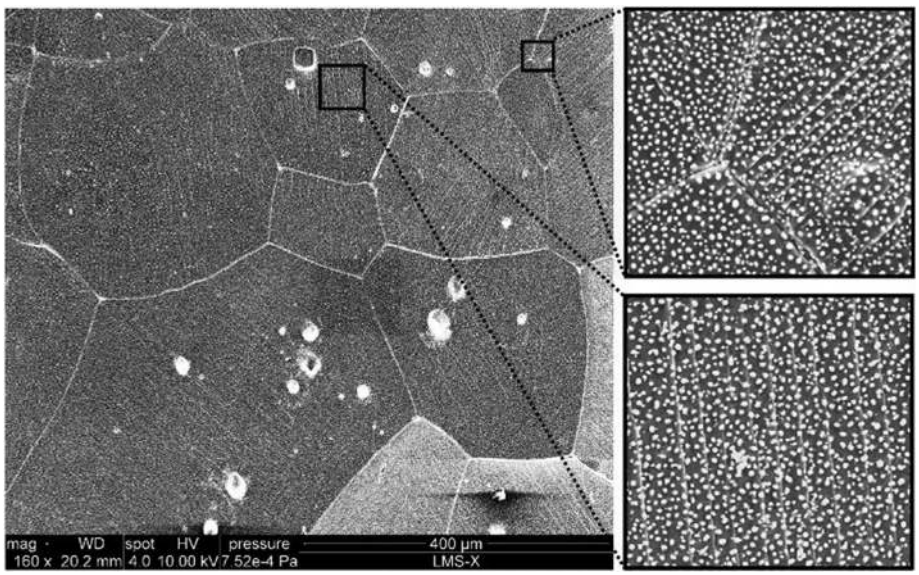

Figure 7. Slip lines observed at the surface of the coarse-grained sample; SEM imaging in secondary electron mode.

size of the microstructure and the type of constitutive behavior. See, e.g., *Salmi et al*. [2012] for a review of proposed definitions. A common way to define the size of an RVE consists in studying the evolutions of the statistical fluctuations of some quantity defined by an averaging procedure over domains of a given size as a function of this size. We adopt such a procedure here. More specifically, we investigate the statistical fluctuations of experimentally measured average strains over domains of a given size as a function of this size, or in other words, the fluctuations of the local strains relative to some gage length ΔL as a function of this length. Fluctuations are quantified by means of the strain distribution function of the von Mises equivalent strain, as well as by its standard deviation. These quantities need to be analyzed over domains that are larger than the RVE size, i.e., over "macroscale" domains, or at least large "mesoscale" domains. Results are plotted in Figure 5: the strain distributions as function of the local strain normalized by the average strain over the investigated ROI are given for four gage lengths, and the continuous evolutions of the standard deviation of the same quantity with respect to gage length are plotted for the three microstructures. Note that because of the very different characteristic sizes of the microstructures, the considered ranges of gage lengths are very different for the three materials. It is clearly observed that, as expected, the fluctuations attenuate when the gage length is enlarged, but they never vanish. A possible quantification of the RVE size consists in choosing the gage length that leads to a standard deviation below 10% of the average strain. With such a choice, it is found that the hot-pressed material seems to be homogeneous for an RVE diameter larger than 1500 μm, while this limit is close to 100 μm for the fine-grained material, and to 2000 μm for the coarse-grained one. These important results permit us to define for each microstructure the pertinent scale for the study of the micromechanisms of deformation. For instance, we verify that the fine-grained samples may be studied at a much finer scale than the other two. This finer scale can only be addressed by SEM investigations. Note also that for the hot-pressed material, the standard deviation of local strains does no longer diminish when the gage length is enlarged above 2.5 mm. This can be explained by the existence of the macroscopic heterogeneity shown in Figure 4 [4] and commented in section 4.1. This macroscale heterogeneity

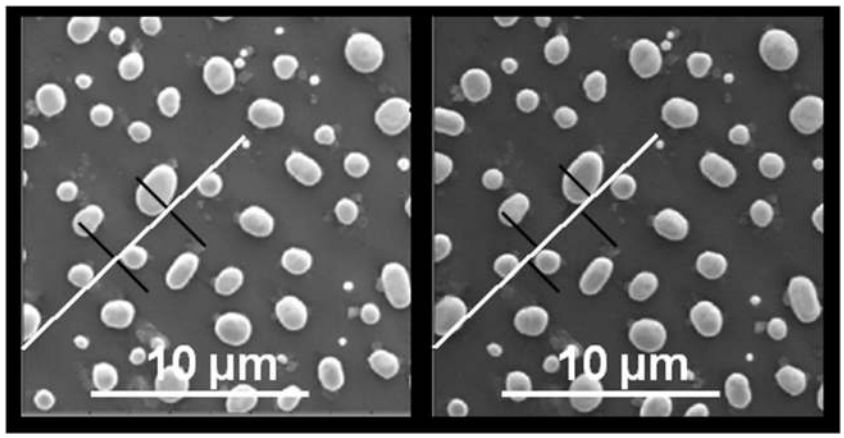

Figure 8. Intragranular plasticity observed at microscale in coarse-grained sample thanks to relative motion of the markers

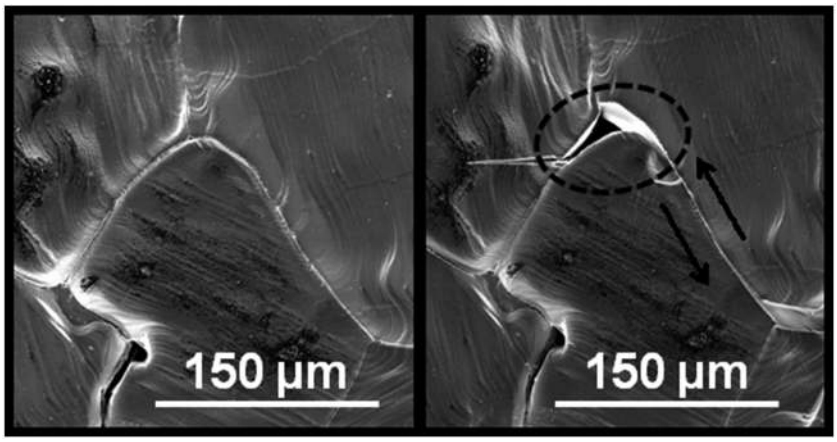

Figure 9. Grain boundary sliding inducing an opening of a cavity at a triple junction in a coarse-grained sample (no markers).

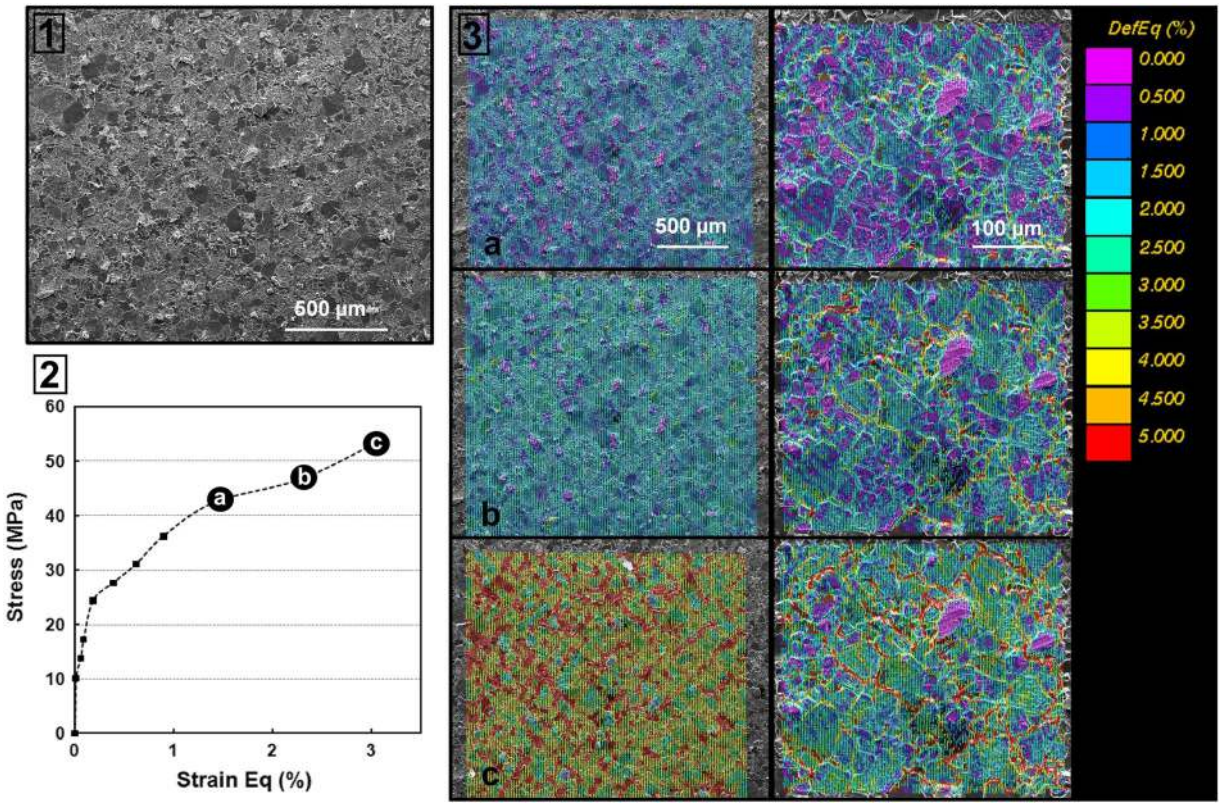

Figure 10. 2D DIC results, equivalent strain from in situ SEM test on fine-grained material at a microscopic scale. (1) Microstructure, (2) macroscopic stress/strain curve, and (3) strains map: Localization along grain boundaries indicates important contribution of GBS to the global deformation.

turned out to be much less pronounced in the other tests for which the areas investigated at macroscale to produce these results were much smaller.

4.3. Coarse-Grained Halite

[40] In this section, one analyzes the local strain fields in the coarse-grained halite. One recalls that this material is characterized by polygonal grains with sizes varying between 250 and 500 µm (Figure 1b) and very low porosity (less than 1%). Two scales of observation have been considered for strain mapping (see Figure 6 and Table 1), covering respectively (almost) the mesoscale of an RVE and a particular microscale field focused on a triple junction, with respective gage lengths of 8 and 1.6 µm. Intracrystalline plasticity is attested both by the observation of slip lines at the surface (Figure 7) and the computation of an intragranular equivalent strain showing discrete bands of deformation within the grains. When the slip direction is parallel to the observation surface, no slip lines are observed in the SEM images, but gliding can be quantified anyway thanks to the displacement of markers and DIC, as illustrated in Figure 8. This mechanism is complemented by grain boundary sliding at some grain boundaries, as illustrated in Figure 9 and by localization near some grain interfaces (Figure 6). In this material both mechanisms do coexist within an RVE as evidenced by the mesoscale maps.

[41] In the considered microscale zoom around a triple junction, plastic slip (CSP) seems to dominate, but some GBS is also observed. Indeed, such very local observations permit to precisely detail the activity of each mechanism and to retrieve the history of their interplay. Referring to grain numbers as noted in Figure 6, we can see at first the activation of plastic deformation (CSP) in grain 1. However, almost at the same time, some deformation is concentrated at the interface between grains 1 and 3; it can be shown to be GBS, probably induced by the crystallographic incompatibility in terms of intragranular crystal plasticity between these grains. At this early stage of deformation, grain 3 behaves in an almost rigid manner. With increasing loads and macroscopic axial deformations, we can observe activation of crystal plasticity in grain 2, while the bands of deformations in grain 1 become more intense and closely spaced. With further loading, grain 3 finally exhibits intragranular plasticity denoted by bands that have almost the same orientation as the bands of deformation in neighboring grain 2.

4.4. Fine-Grained Material

[42] The fine-grained material needs to be observed at a much finer scale because of its grain size,which is in the interval between 30 and 80 µm. Again, two scales are considered (see Figure 10 and Table 1), with corresponding gage lengths of 18 and 6 µm, respectively. But now, the larger view should be considered as a high definition "macroscale" field, while the smaller one is a "large mesoscale" view (scale in excess of the previously defined mesoscale). Note that the DIC data of the larger scale have been used to

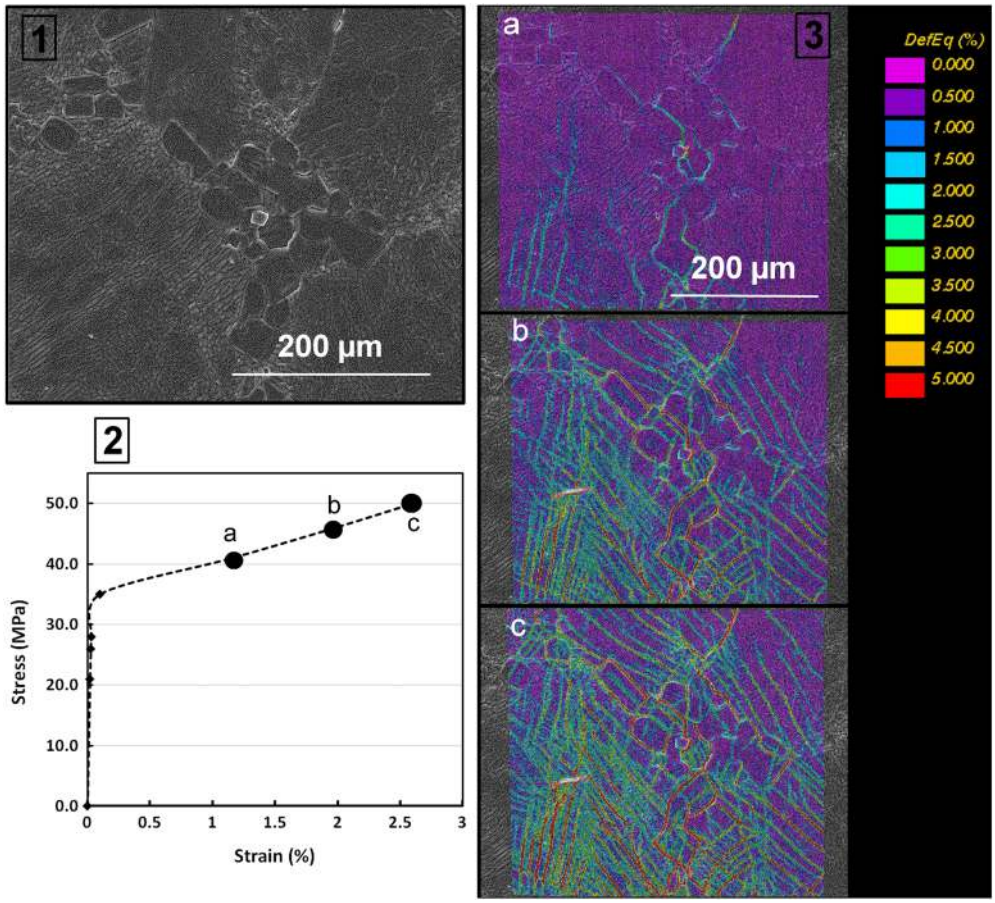

Figure 11. 2D DIC results from in situ SEM test on hot pressed material. (1) Microstructure, (2) macroscopic stress/strain curve, and (3) strain maps given in equivalent strain.

construct the plots on the right side of Figure 5. The heterogeneity at macroscale appears in the form of deformation bands qualitatively similar to those observed at macroscale in the hot-pressed bimodal material (see section 4.1), but with much smaller characteristic sizes. No significant purely macroscopic heterogeneity is observed however, which explains the continuous decrease of the standard deviation of local strain with gage length as shown in Figure 5.

[43] This macroscale view does however not allow a clear identification of the mechanisms that are active at the microscale and contribute to the observed strong heterogeneity. This information is provided by the mesoscale data, in which both microstructure and strain field are spatially better resolved. At this scale, it becomes clear that this material presents the same micromechanisms of deformation as the coarse-grained one: both intracrystalline plasticity and grain boundary sliding. However, some differences can be noticed: bands of deformation appear to be more localized on the grain boundaries and strain seems to be less intense inside grains, which indicates that GBS is likely be more predominant in this material. It is noteworthy that this material was not marked by gold spheres because, owing to the fine-grained microstructure, there was enough local contrast. Therefore, the local information is less precise than for the coarse-grained material and individual slip bands are less visible. The largest grains however clearly show a few slip bands evidencing a CSP contribution.

4.5. Bimodal Grain Size Distribution (Hot-Pressed)

[44] The two previously studied microstructures had a common property: a unimodal grain size distribution. The hot-pressed material presented in this section is made of both coarse and fine grains. The macroscale strain heterogeneity has already been characterized in this material in section 4.1. Let us now focus on a "small mesoscale", with a pixel size of about 0.2 µm, a correlation window of 15 × 15 pixels, yielding a gage length of about 3 µm. The observed area covers a group of small grains surrounded by four large ones, and will be used to investigate how the total strain is partitioned between each class of grain sizes. Results of DIC (Figure 11) show predominant intracrystalline plasticity within the large grains and well-marked grain sliding at grain boundaries in the fine-grained domain. Inside the fine grains, we observe only very few bands of deformation (about one or two). The importance of the grain size distribution on the activation of the different mechanisms is thus well illustrated with this mixed mode material.

5. Discussion

5.1. Microstructure and Deformation Mechanisms

[45] We recall that the term microstructure essentially refers here to grain size distribution and crystalline

orientation. Our results from SEM observations and application of the DIC method have shown the occurrence of two main mechanisms of deformation: intracrystalline plasticity and grain boundary sliding (GBS) with a respective importance closely linked to the microstructure. Indeed, for the coarse-grained material, we observe directly many surface slip lines and through DIC computations, a lot of intracrystalline bands of deformation, which attests of dominant crystal plasticity in many grains, but we also notice many grains that appear much less deformed. Those grains may be termed incompatible: their crystallographic orientation and the local state of stress do not permit an easy activation of slip systems. In these instances, a relative displacement along grain boundaries is activated as a local accommodation mechanism. The fine-grained material presents the same mechanisms but with a much more pronounced localization of the deformation near the grain boundaries. The latter include both localization inside the grains and at the interfaces themselves. We suggest that for this microstructure, GBS plays a more important role owing to the larger proportion of interfaces inherent to a fine-grained structure. The detailed analysis, at fine microscale, of the details of this GBS deformation mode has however not yet been done, because it would require an investigation of local strain fields relative to submicrometric gage lengths, for which our experimental procedure is not yet well suited, essentially because of the lack of an appropriate marking of nanometric size. Work is under progress along this line. The few bands of deformation observed in small grains, when compared to a much larger amount of bands in coarse grains may clearly be linked to a grain size effect on CSP. In a general sense, slip bands self-organize with a regular interspacing, which suggests an internal length scale for the distribution of dislocations with alternating strain-free (defect-free) bands and bands of strong localization denoting the activity of a slip plane. Conversely, very few localized bands appear inside fine grains, which suggests a strong interaction between self organizing slip bands and grain boundaries. This observation agrees with the Hall-Petch effect [*Hall*, 1951; *Petch*, 1953], which corresponds to limitation of CSP with decreasing grain size (yield stress proportional to $d^{-1/2}$, where d is the grain size) due to the simultaneous decrease of the mean free gliding distance with the presence of numerous interfaces. In this case the strain tends to localize near the interfaces either by GBS or CSP involving only a fraction of the grain and possibly several slip systems (multiple glide), in contrast with the interior of larger grains, where only one or two slip systems seem to be simultaneously active. These observations highlight the fact that interfaces strongly influence the local stress states. To further understand the interplay between CSP, GBS, and microstructures, the next step is to quantify the respective contributions of each mechanism. This procedure cannot be reduced to a purely mathematical development since in its application, it edges on the multiscale nature of what may be defined as strain for heterogeneous materials. An illustration of this important question is presented in the next subsection.

5.2. Multiscale Structure of Deformation and Gage Length

[46] The multiscale nature of strain in heterogeneous material as will be demonstrated in the following, renders impossible the direct application of the classical concept of deformation gradient of continuum mechanics, as defined by equations (3) and (5), as already suggested in section 3.5. Let us for instance consider the estimated strain fields for the hot-pressed material, at various gage lengths : $\Delta L \approx 2$ mm (Figure 4 [4]), $\Delta L \approx 0.2$ mm (Figure 4 [3]), and $\Delta L \approx 3$ μm (Figure 11). These are different views of the same deformed material, with very different aspects. With a large gage length (Figure 4 [4]) one does not see the local strain heterogeneities (4 Figure 4[3]); one only sees the heterogeneity related to the macroscopic loading conditions, two large conjugate deformation bands. A much closer view near a slip line like in Figure 8 would show a very discontinuous strain map, with discrete narrow slip bands similar to those on the right side of Figure 6 [3]. Let one consider now the strain at a material point **X**, located between two slip bands, within a grain of the microstructure studied on Figure 4. For a large gage length ΔL, its value is given by the strain map in Figure 4 [4]. With decreasing gage lengths, the strain would evolve and successively take the values plotted in the other figures mentioned above Figures 4 [3] and 11 [3]. At the end, for a very small gage length, smaller than the distance between two slip bands, the strain would almost vanish, because the material in the vicinity of **X** deforms only elastically. Conversely, if one now considers another material point located exactly on one of the adjacent slip bands, a few micrometers away from the previous point, the strain at large gage length would remain the same, but at very small gage length it would tend to infinity, because of the discontinuity of displacement across the slip line, as illustrated in Figure 8. This demonstrates the critical importance of the precise definition of gage lengths when local strains are to be experimentally characterized, and of course also when experimental strain fields are compared to each other or to results of numerical models.

5.3. Relative Contributions of Crystal Plasticity and Grain Boundary Sliding

[47] Crystal plasticity and GBS both contribute to the global plastic deformation and act almost concomitantly albeit in different parts of a sample and with a strong dependence on the microstructure, as shown qualitatively in section 4. The objective of this section is to outline a method to quantify their respective importance and present preliminary results.

5.3.1. Principle of the Quantification

[48] The principle of this quantification can be found in *Rupin* [2006] for the simpler case of a two-phase stainless steel. We adapt it here to a crystalline material, with potential GBS. Let us consider (see Figure 12) a domain Ω made of parts of two adjacent grains separated by an interface I, $\Omega = \Omega^+ \cup \Omega^-$, specifying the domains occupied by each grain. If there is no interface sliding, the average deformation gradient over the domain Ω is

$$< \mathbf{F} >_{\Omega} = \frac{|\Omega^+|}{|\Omega|} < \mathbf{F} >_{\Omega^+} + \frac{|\Omega^-|}{|\Omega|} < \mathbf{F} >_{\Omega^-}, \qquad (15)$$

where $|\Omega|$ is the measure of domain Ω. The resulting average deformation gradient is thus a weighed sum of the average deformation gradient in each grain. If there is GBS at the interface I, there is an additional contribution $\Delta\mathbf{F}$, which may

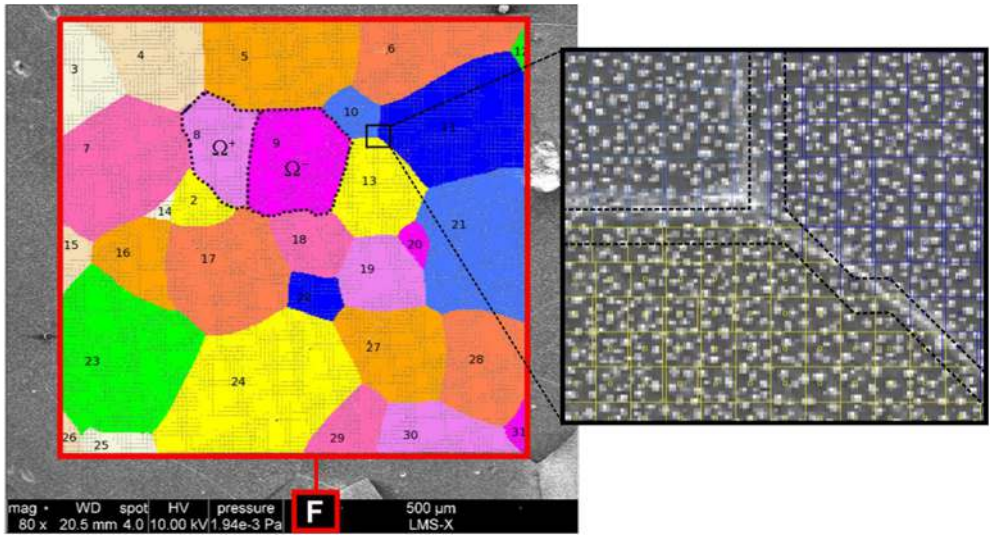

Figure 12. Identification of the different phase in the polycrystal and computation of average contribution of GBS to overall gradient with CMV.

be expressed as a function of the displacement discontinuity across the interface.

$$\Delta \mathbf{F} = \int_I [[\mathbf{u}]] \otimes \mathbf{n} ds, \tag{16}$$

where $[[\mathbf{u}]] = \mathbf{u}^+ - \mathbf{u}^-$ is the displacement jump across the interface I of normal $\mathbf{n}$ oriented from the "–" towards the "+" side. Equation (15) becomes

$$< \mathbf{F} >_\Omega = \frac{|\Omega^+|}{|\Omega|} < \mathbf{F} >_{\Omega^+} + \frac{|\Omega^-|}{|\Omega|} < \mathbf{F} >_{\Omega^-} + \Delta \mathbf{F}. \tag{17}$$

[49] This concept is easily generalized by considering that each grain g, occupying domain Ω^g, constitutes a phase (Figure 12), and by calculating the average deformation gradients within each grain, without considering the interfaces, for each grain in the ROI Ω, at each step of the deformation. Note that for grains at the boundary of the ROI, only the part of the grain inside the ROI is considered. The global deformation gradient is also computed, and the contribution of the interfaces is obtained as the difference between the overall gradient and the weighted average of the average deformation gradients within all grains in the ROI

$$\Delta \mathbf{F} = < \mathbf{F} >_\Omega - \sum_{\text{all grains } g} \frac{|\Omega^g|}{|\Omega|} < \mathbf{F} >_g. \tag{18}$$

5.3.2. Implementation and Results

[50] The practical implementation is based on the calculation of the averages $< \mathbf{F} >_\Omega$ and $< \mathbf{F} >_g$ with the method described at the end of section 3.5: contours defined by DIC measurement points encompassing the whole ROI, or only a particular grain g and based on measurement points strictly inside the considered grain, as illustrated by the dashed black line in Figure 12, are considered. See also *Allais et al*. [1994] for similar considerations. Such a quantitative evaluation needs to be performed over a statistically representative domain. The RVE that is defined here is not the same as an RVE representative of global mechanical properties. One needs only enough grains and interfaces to observe a sampling statistically representative of the activity of both mechanisms (CSP and GBS). To this end, the mesoscale domains described in section 4 have been considered. The geometry of the grains may be determined directly from the SEM micrographs or from electron back scatter diffraction measurements not detailed here.

[51] This quantification has been performed for the various tested microstructures. It clearly confirms that the interfaces carry a large proportion of the total deformation (more than 50%) for the fine-grained material. For the large-grained one, intragranular CSP is the dominant mechanism and contributes to more than 80% of the total strain.

[52] These quantitative data should however be taken with care at this stage. In the principle of quantification, the interface is idealized as a surface of discontinuity. However, in the actual measurements, owing to their discrete nature, there is a domain near the grain boundaries (the area between the black dashed lines in Figure 12), of very small but nonzero measure, which is not associated to any grain and where some complex CSP may take place as well as GBS. The part of the deformation attributed to GBS encompasses this contribution of CSP, and is thus likely to be slightly overestimated by the present approach. In addition, DIC measurements at the positions used to compute the contour integrals in the grains are based on correlation windows, which may spread over the neighboring grains, so that displacement evaluation might be inaccurate. It is difficult to evaluate precisely the errors associated to these limitations. Work is currently under progress to modify the DIC formulation to address this question.

6. Conclusion

[53] We have shown that crystal slip plasticity is the major strain accommodation mechanism. However, we have also observed that crystal plasticity incompatibilities due to the relative orientations of neighboring grains and the local stress state induce local interfacial microcracking and GBS, which in turn results in progressive accumulation of damage, leading ultimately to macroscopic shear fracturing.

Although crystal slip is for some microstructures the main deformation mechanism, GBS is always present in the observed crystals, and in some cases, such as fine grained materials, GBS may even be a dominant deformation mode. It appears that at room temperature and in the strain rate range that has taken place (say about $\dot{\varepsilon} \approx 10^{-4} s^{-1}$, although, owing to local heterogeneity it may widely differ), crystal plasticity and GBS are cooperational mechanisms, and hence, that the macroscopic viscoplastic flow and the local interfacial damage are intimately linked. As a consequence, modeling long-term flow behavior of salt should account for these physical phenomena, but also very likely include some interfacial healing mechanism.

[54] **Acknowledgments**. This work has been supported by both the chair "Energies durables" of Ecole Polytechnique, sponsored by EDF and CEA, and the cooperative project "MicroNaSel" funded by the Agence Nationale de la Recherche (ANR). The SEM in situ experiments were performed with the FEI Quanta 600 FEG-SEM available at LMS, which has been acquired with the combined financial support of Region Ile de France ("SESAME 2004" program), Ecole polytechnique and CNRS. We also thank D. Caldemaison, H. Gharbi, V. de Greef, A. Tanguy, P. Valli, and D. Yang for their help and assistance to run the experiments.

References

Allais, L., M. Bornert, T. Bretheau, and D. Caldemaison (1994), Experimental characterization of the local strain field in a heterogeneous elastoplastic material, *Acta Metallurgica et materialia*, *42*(11), 3865–3880.

Bérest, P., P. A. Blum, J. P. Charpentier, H. Gharbi, and F. Valés (2005), Very slow creep tests on rock samples, *Int. J. Rock Mech. Min.*, *42*(4), 569–576.

Bornert M., F. Brémand, P. Doumalin, J. C. Dupré, M. Fazzini, M. Grédiac, F. Hild, J. Molinard, and J. J. Orteu (2009), Assessment of digital image correlation measurement errors: Methodology and results, *Exp. Mec.*, *49*(3), 353–370.

Bornert M., F. Valés, H. Gharbi, and D. Nguyen Minh (2010), Multiscale full-field strain measurements for micromechanical investigations of the hydromechanical behaviour of clayey rocks, *Strain*, *46*, 33–46.

Bornert, M., J. J. Orteu, and S. Roux, (2011), Corrélation d'images, in Mesures de champs et identification, Grédiac, M. and Hild, F. Eds., Hermès Science, Chap. 6, 175–208.

Carter, N. L. and F. D. Hansen (1983), Creep of rocksalt, *Tectonophysics*, *92*(4), 275–333.

Crotogino, F., K-U. Mohmeyer, and R. Scharf (2001), *Huntorf CAES: More Than 20 Years of Successful Operation*, Spring 2001 Meeting Orlando, Florida, USA 15-18 April 2001.

Dautriat, J., M. Bornert, N. Gland, A. Dimanov, and J. L. Raphanel (2011), Localized deformation induced by heterogeneities in porous carbonate analysed by multi-scale digital image correlation, *Tectonophysics*, *503*, 100–116.

de Meer, S., C. J. Spiers, C. J. Peach and T. Watanabe (2002) Diffusive properties of fluid-filled grain boundaries measured electrically during active pressure solution, *Earth and Planet Sci. Lett.*, *200*, 147–157.

Desbois, G., P. Závada, Z. Schléder and J. L. Urai (2010) Deformation and recrystallization mechanisms in actively extruding salt fountain: Microstructural evidence for a switch in deformation mechanisms with increased availability of meteoric water and decreased grain size (Qum Kuh, central Iran), *protect J. Struct. Geol.*, *32*(4), 580–594.

Dimanov, A., M. P. Lavie, G. Dresen, J. Ingrin, and O. Jaoul (2003) Creep of polycrystalline anorthite and diopside, *J. Geophys. Res.*, *108 B1* article 2061.

Doumalin, P. and M. Bornert (2000) Micromechanical applications of digital image correlation techniques. Interferometry in Speckle Light, Theory and Applications Jacquot, P. and Fournier, J.M., Eds., Springer, Berlin, Heidelberg, 67–74.

Doumalin, P., M. Bornert and J. Crépin (2003), Caractérisation de la répartition de la déformation dans les matériaux hétérogènes, *Mécanique et industrie*, *4*, 607–617.

Dresen, G. and B. Evans (2009), Brittle and semibrittle deformation of synthetic marbles composed of 2 phases, *J. Geophys. Res.*, *98*(B7), 11921–11933.

Franssen, R. C. M. W. (1994), The rhelogy of synthetic rocksalt in uniaxial compression, *Tectonophysics*, *223*, 1–40.

Gérard, C., F. N'Guyen, N. Osipov, G. Cailletaud, M. Bornert, and D. Caldemaison (2009), Comparison of experimental results and finite element simulation of strain localization scheme under cyclic loading, *Comp. Mater. Sci.*, *46*(3), 755–760.

Hall, E. O. (1951), The deformation and aging of mild steel. 3. discussion and results, *Proc. Phys. Soc. of London*, *B64-381*, 747–753.

Hedan, S., P. Cosenza, P. Valle, P. Dudoignon, A.L. Fauchille and J. Cabrera (2012), Investigation of the damage induced by desiccation and heating of Tournemire argillite using digital image correlation, *Int. J. Rock Mech. Min.*, *51*, 64–75.

Ter Heege, J. H., J. H. P. De Bresser, and C. J. Spiers (2005), Dynamic recrystallization of wet synthetic polycrystalline halite: dependence of grain size distribution on flow stress, temperature and strain, *Tectonophysics*, *396*, 35–57.

Héripré, E., M. Dexet, J. Crépin, L. Gélebart, A. Roos, M. Bornert, and D. Caldemaison (2007), Coupling between experimental measurements and polycrystal finite element calculations for micromechanical study of metallic materials, *Int. J. Plasticity*, *23*(9), 1512–1539.

Hickman, S. and B. Evans (1995), Kinetics of pressure solution at halite-silica interfaces and intergranular clay films, *J. Geophys. Res..*, *100*, 13,113–13,132.

Langer, M. (1984), The rheological behavior of rock salt, *Proc. 1st International Conference on the Mechanical Behavior of Salt*, Trans Tech Publications, Clausthal-Zellerfeld, Germany, 201–240.

Lebensohn, R. A., P. R. Dawson, H. M. Kernc, and H. R. Wenk (2003), Heterogeneous deformation and texture development in halite polycrystals: comparison of different modeling approaches and experimental data, *Tectonophysics*, *370*(1-4), 287–311.

Liu, Y., P. Gilormini, and P. Ponte Castañeda (2005), Homogenization estimates for texture evolution in halite, *Tectonophysics*, *406*(3-4), 179–195.

Malvern, L. E. (1969), Introduction to the mechanics of a continuum medium. Prentice-Hall, Inc., Englewood Cliffs, NJ USA.

Martin, B., K. Roller, and B. Stockhert (1996), Low-stress pressure solution experiments on halite single-crystals, *Tectonophysics*, *308*(Issue 3, 15), 299–310.

Peach, C. J. and C. J. Spiers (1996), Influence of crystal plastic deformation on dilatancy and permeability development in synthetic salt rock, *Tectonophysics*, *256*(1-4), 101–128.

Petch, N. J. (1953), The cleavage strength of polycrystals, *J. Iron Steel.*, *174-1*, 25–28.

Rupin, N. (2006), Déformation à chaud de métaux biphasés: modélisation théoriques et confrontations expérimentales. PhD thesis, Ecole Polytechnique.

Salençon, J. (2001), Handbook of continuum mechanics: general concepts, thermoelasticity. Translated by Stephen Lyle. Springer, Berlin New York Paris.

Salmi, M., F. Auslender, M. Bornert, and M. Fogli (2012), Various estimates of Representative Volume Element sizes based on a statistical analysis of the apparent behavior of random linear composites, *Comptes-rendus Mécanique*, *340*(4-5), pp. 230-246.

Schenk, O., J. L. Urai, and S. Piazolo (2006), Structure of grain boundaries in wet, synthetic, polycrystalline, statically recrystallizing halite: evidence from cryo-sem observations, *Geofluids*, *6*, 93–104.

Schléder, Z., S. Burliga, and J. L. Urai (2007), Dynamic and static recrystallization-related microstructures in halite samples from the Klodawa salt wall (central Poland) as revealed by gamma-irradiation, *Neues Jahrbuch für Mineralogie-Abhandlungen*, *184*(1), 17–28.

Senseny, P. E., F. D. Hansen, J. E. Russell, N. L. Carter, and J. W. Handin (1992), Mechanical behaviour of rock salt: Phenomenology and micromechanisms, *Int. J. Rock Mec. Min.*, *29*(4), 363–378.

Spiers, C. J., and P. M. T. M. Schutjens (1999), Intergranular pressure solution in NaCl: Grain-to-grain contact experiments under the optical microscope.*Oil and Gas Science and Technology - Revue IFPEN*, *54*(6), 729–750.

Sutton, M. A., W. J. Wolters, W. H. Peters, W. F. Ranson, and S. R. McNeill (1983), Determination of displacement using an improved digital correlation method, *Image Visual. Comput.*, *1*(3), 133–139.

Sutton, M. A., J.-J. Orteu, and H. W. Schreier (2009), Image correlation for shape, motion and deformation measurements: basic concepts, theory and applications. Springer Science+Business Media, New York.

Skvortsova, Z. N. (2003), Deformation by the mechanism of dissolution-reprecipitation as a form of adsorption plasticization of natural salts, *Colloid J.*, *66*, 1–10.

Tatschl, A., and O. Kolednik (2003), On the experimental characterization of crystal plasticity in polycrystals, *Mater. Sci. Eng.*, *A342*, 152–168.

Urai, J. L., C. J. Spiers, R. C. Peach, M. W. Franssen, and J. L. Liezenberg (1987), Deformation mechanisms operating in naturally deformed halite rocks as deduced from microstructural investigations, *Geologie en Mijnbouw*, *66*, 165–176.

Urai, J. L., C. J. Spiers, H. J. Zwart, and G. S. Lister (1986), Weakening of rock salt by water during long term creep, *Nature*, *324*, 534–557.

Watanabe, T. (2010), Geometry of intercrystalline brine in plastically deforming halite rocks: inference from electrical resistivity, *Geological Society, London, Special Publications*, *332*, 69–78.

Wang, Y. Q., M. A. Sutton, H. A. Bruck, and H. W. Schreier (2009), Quantitative error assessment in pattern matching: effects of intensity pattern noise, interpolation, strain and image contrast on motion measurements, *Strain*, *45*, 160–178.

Wenk, H. R., M. Armann, L. Burlini, K. Kunze, and M. Bortolotti (2009), Large strain shearing of halite: Experimental and theoretical evidence for dynamic texture changes, *Earth and Planet Sci. Lett.*, *280*(1-4), 205–210.

Wenk, H. R., G. Canova, A. Molinari, and H. Mecking (1989), Texture development in halite: Comparison of Taylor model and self-consistent theory, *Acta Met*, *37*(7), 2017–2029.

Yang, D.S., M. Bornert, H. Gharbi, P. Valli, and L. Wang (2010), Optimized optical setup for DIC in rock mechanics Proc. of *14th International Conference on Experimental Mechanics (ICEM14)*, EPJ Web of Conferences, Vol. 6, Art. Nr. 22019.

Yang, D.S., M. Bornert, S. Chanchole, H. Gharbi, P. Valli, and B. Gatmiri (2012), Dependence of elastic properties of argillaceous rocks on moisture content investigated with optical full-field strain measurement techniques, *Int. J. Rock Mining & Mining Sci.*, *53*, 45–55.